

Pushing the Limits: Hydrothermally Synthesized $\text{Bi}_2\text{MnCoO}_6$ Electrodes with Exceptional Cyclability for Asymmetric Supercapacitors

Shivam Kumar Mittal, Amiya Mandal, Deepanshu Kaneria, Udeshwari Jamwal, and Kanhaiya Lal Yadav*

Perovskite oxides are revolutionizing energy storage with their robust stability and versatile redox chemistry. Here, a novel bismuth-based double perovskite, $\text{Bi}_2\text{MnCoO}_6$ (BMCO), is introduced as a next-gen supercapacitor electrode, synthesized via a hydrothermal synthesis. The strategic placement of Bi^{3+} at the A-site imparts superior electronic conductivity and ion transport. Simultaneously, the Mn/Co B-site duo unlocks a rich, reversible redox palette ($\text{Mn}^{2+/3+/4+}$, $\text{Co}^{2+/3+}$), driving exceptional pseudocapacitance. In three-electrode tests, BMCO delivers an impressive 627 F g^{-1} specific capacitance at 0.5 Ag^{-1} and maintains near-ideal reversibility. Pushing the material into a real device, an asymmetric supercapacitor (ASC) is assembled by pairing BMCO as the cathode with activated carbon anode in

6 M KOH and achieves a 23 Wh kg^{-1} energy density and up to 14 kW kg^{-1} power density. Most strikingly, the BMCO//AC ASC endures 100,000 charge–discharge cycles at 5 Ag^{-1} with $\approx 100\%$ Coulombic efficiency. A pronounced “self-activation” in the first 10,000 cycles boosts capacitance to 150%, as electrolyte penetration unlocks hidden redox sites. Thereafter, the device stabilizes at $\approx 120\%$ of its original capacitance, proving remarkable long-term durability, setting a new benchmark for perovskite-based ASCs. This work not only elevates perovskite materials into the forefront of high-performance supercapacitors but also demonstrates how precision cation design and eco-friendly hydrothermal processing can yield ultra-stable energy storage solutions.

1. Introduction

The escalating global demand for efficient and sustainable energy storage solutions, driven by the proliferation of portable electronics, electric vehicles, and renewable energy systems, has intensified research into advanced electrochemical energy storage devices.^[1–3] Among these, supercapacitors have garnered significant attention due to their high-power density, rapid charge–discharge capabilities, and exceptional cycle life.^[4–8] However, their relatively low energy density compared to batteries remains a limitation, necessitating the exploration of novel electrode materials that can enhance energy storage performance. Supercapacitors are broadly classified into electric double-layer capacitors (EDLCs) and pseudocapacitors, based on their charge storage mechanisms.^[9] EDLCs store energy through electrostatic adsorption of ions at the electrode–electrolyte interface, while pseudocapacitors involve fast and reversible faradaic

redox reactions at or near the electrode surface.^[10–15] Transition metal oxides, with their multiple oxidation states, have been extensively studied as pseudocapacitive materials due to their high theoretical capacitance and rich redox chemistry but suffer from low capacities, high cost, or narrow potential window.^[16–20]

In this regard, Perovskite oxides, characterized by the general formula ABO_3 , have emerged as promising candidates for supercapacitor electrodes owing to their structural versatility, thermal stability, and tunable electronic properties.^[21–24] Extending this family, double perovskites ($\text{A}_2\text{BB}'\text{O}_6$) offer enhanced flexibility by accommodating two different transition metals at the B-site, enabling synergistic interactions that can improve electrochemical performance. The incorporation of dual B-site cations facilitates multiple redox processes, enhances electronic conductivity, and provides improved ion diffusion pathways, all of which are critical for high-performance supercapacitor electrodes.^[25–27] One of the distinctive characteristics of these compounds lies in the structural stability of their cationic framework, which can accommodate oxygen vacancies that serve as active sites for charge storage.^[28,29] While this class of materials has been widely investigated for energy conversion applications, their potential for charge storage remains relatively underexplored in the literature.^[30–33] Recent studies have demonstrated the potential of various perovskite and double perovskite oxides in energy storage applications. For instance, Pan et al. reported the use of BiFeO_3 nanoflakes as pseudocapacitor electrodes, achieving a specific capacitance of 456 F g^{-1} .^[34] Yin et al. developed BiFeO_3 nanoplates via an efficient hydrothermal method,

S. K. Mittal, A. Mandal, D. Kaneria, K. L. Yadav

Smart Materials Research Laboratory
Department of Physics
Indian Institute of Technology Roorkee
Roorkee 247667, India
E-mail: klyadav35@gmail.com

U. Jamwal
National University of Singapore
5A Engineering Drive 1, 117411, Singapore

 Supporting information for this article is available on the WWW under <https://doi.org/10.1002/batt.202500706>

which exhibited a C_s of 254 F g^{-1} at 1 mV s^{-1} and demonstrated good cycling stability, retaining 84% of its initial capacitance after 1000 cycles.^[35] Similarly, Wang et al. synthesized spherical Bi_2WO_6 structures for use in supercapacitors, reporting a C_s of 412 F g^{-1} at 0.5 mA cm^{-2} .^[36] In another study, Botha et al. fabricated BiFeO_3 nanoparticles using a green synthesis approach and obtained a C_s of 105 F g^{-1} at 0.25 A g^{-1} .^[37] However, its practical application is hindered by poor conductivity, limited surface area, and cycling stability, which restrict its performance in supercapacitor applications.^[38]

In this study, we introduce $\text{Bi}_2\text{MnCoO}_6$ (BMCO), a bismuth-based double perovskite oxide, as a novel electrode material for supercapacitor applications. The presence of Bi^{3+} at the A-site contributes to enhanced electronic conductivity and structural distortion, facilitating ion diffusion and improving electrochemical kinetics.^[39,40] The B-site cations, Mn and Co, exhibit multiple accessible oxidation states ($\text{Mn}^{2+/3+/4+}$ and $\text{Co}^{2+/3+}$), providing a broad redox window and contributing to higher pseudocapacitive performance. BMCO was synthesized via a hydrothermal method that allows for the controlled growth of nanostructured oxide materials with desirable features such as high crystallinity, uniform particle morphology, and enhanced surface area. Unlike traditional solid-state synthesis, hydrothermal routes are particularly advantageous for preserving metastable structures and incorporating mixed-valence states—key factors in optimizing pseudocapacitive behavior.

To evaluate the practical viability of BMCO, an asymmetric supercapacitor (ASC) was fabricated using BMCO as the positive electrode and commercial activated carbon (AC) as the negative electrode. This asymmetric configuration leverages the high pseudocapacitance of BMCO and the EDLC behavior of AC to widen the operating voltage window and enhance overall energy density. The BMCO//AC device delivered high C_s , excellent rate capability, and remarkable long-term cycling stability, retaining a large fraction of its initial capacitance after several thousand charge-discharge cycles. The outstanding performance of BMCO can be attributed to the synergistic redox activity of Mn and Co, the structural integrity of the double perovskite lattice, and the favorable morphology obtained through hydrothermal synthesis. This study not only introduces a new member to the growing class of perovskite-based supercapacitor materials but also highlights the importance of strategic cation selection and soft-chemical synthesis in designing next-generation energy storage devices.

2. Experimental Section

2.1. Chemicals Used

All reagents used in this work were of analytical grade and utilized as obtained, without undergoing any further purification steps. For the synthesis of $\text{Bi}_2\text{MnCoO}_6$ (BMCO), bismuth(III) nitrate pentahydrate [$\text{Bi}(\text{NO}_3)_3 \cdot 5\text{H}_2\text{O}$], manganese(II) nitrate hexahydrate [$\text{Mn}(\text{NO}_3)_2 \cdot 6\text{H}_2\text{O}$, HiMedia], cobalt(II) nitrate hexahydrate [$\text{Co}(\text{NO}_3)_2 \cdot 6\text{H}_2\text{O}$, HiMedia], and urea ($\text{CO}(\text{NH}_2)_2$) were used as

starting precursors. Additional reagents and materials employed during electrode fabrication and electrochemical analysis included N-methyl-2-pyrrolidone (NMP, 99% pure, RANKEM), polyvinylidene difluoride (PVDF), carbon black (Super P), exfoliated graphite, sodium hydroxide (NaOH, QUALIGENS), potassium hydroxide (KOH, EMPARTA), and polyvinyl alcohol (PVA, HiMedia). Pure deionized (DI) water was used as the primary solvent for all dispersions, solution preparations, and washing steps throughout the synthesis and fabrication processes.

2.2. Methodology

The BMCO nanostructured material was synthesized via a hydrothermal method using stoichiometric amounts of metal nitrates and urea in DI water as the reaction medium. In a typical synthesis procedure, 1 mmol of bismuth(III) nitrate pentahydrate, 0.5 mmol of manganese(II) nitrate hexahydrate, and 0.5 mmol of cobalt(II) nitrate hexahydrate were accurately weighed and dissolved in 70 mL of DI water under constant magnetic stirring. Subsequently, 2 mmol of urea was added to the solution, serving as a slow-releasing source of hydroxide ions to facilitate uniform nucleation and growth of the desired phase. To support *in situ* growth of the active material, a piece of cleaned nickel foam ($1 \times 1 \text{ cm}^2$) was immersed in the precursor solution. The entire mixture was then transferred into a 100 mL Teflon-lined stainless steel autoclave, sealed tightly, and subjected to hydrothermal treatment at 140°C for 8 h in a hot air oven. After natural cooling to room temperature, the resulting product was collected, and the nickel foam was carefully removed and washed several times with DI water and absolute ethanol to eliminate any residual precursors or loosely bound particles. The washed product was then dried overnight at 60°C in a hot air oven. Finally, the dried sample was subjected to calcination at 350°C for 3 h in a muffle furnace to improve crystallinity and ensure phase formation of the double perovskite $\text{Bi}_2\text{MnCoO}_6$. A schematic representation of the synthesis process is presented in Figure 1(a).

3. Results and Discussion

3.1. Morphological and Elemental Analysis

The surface morphology of the synthesized $\text{Bi}_2\text{MnCoO}_6$ (BMCO) nanostructures was investigated using field emission scanning electron microscopy (FE-SEM), as shown in Figure 1b–1d. The low to high magnification images reveal a porous, interconnected network of nanofibrous structures uniformly coated over the surface of the nickel foam substrate. At lower magnification Figure 1b, the electrode surface appears to be completely covered with a dense mat of fibrous material, suggesting good adherence of the active material to the current collector. With increasing magnification Figure 1c and d, the fibrous morphology becomes more pronounced, highlighting the formation of entangled nanofibers, which are advantageous for

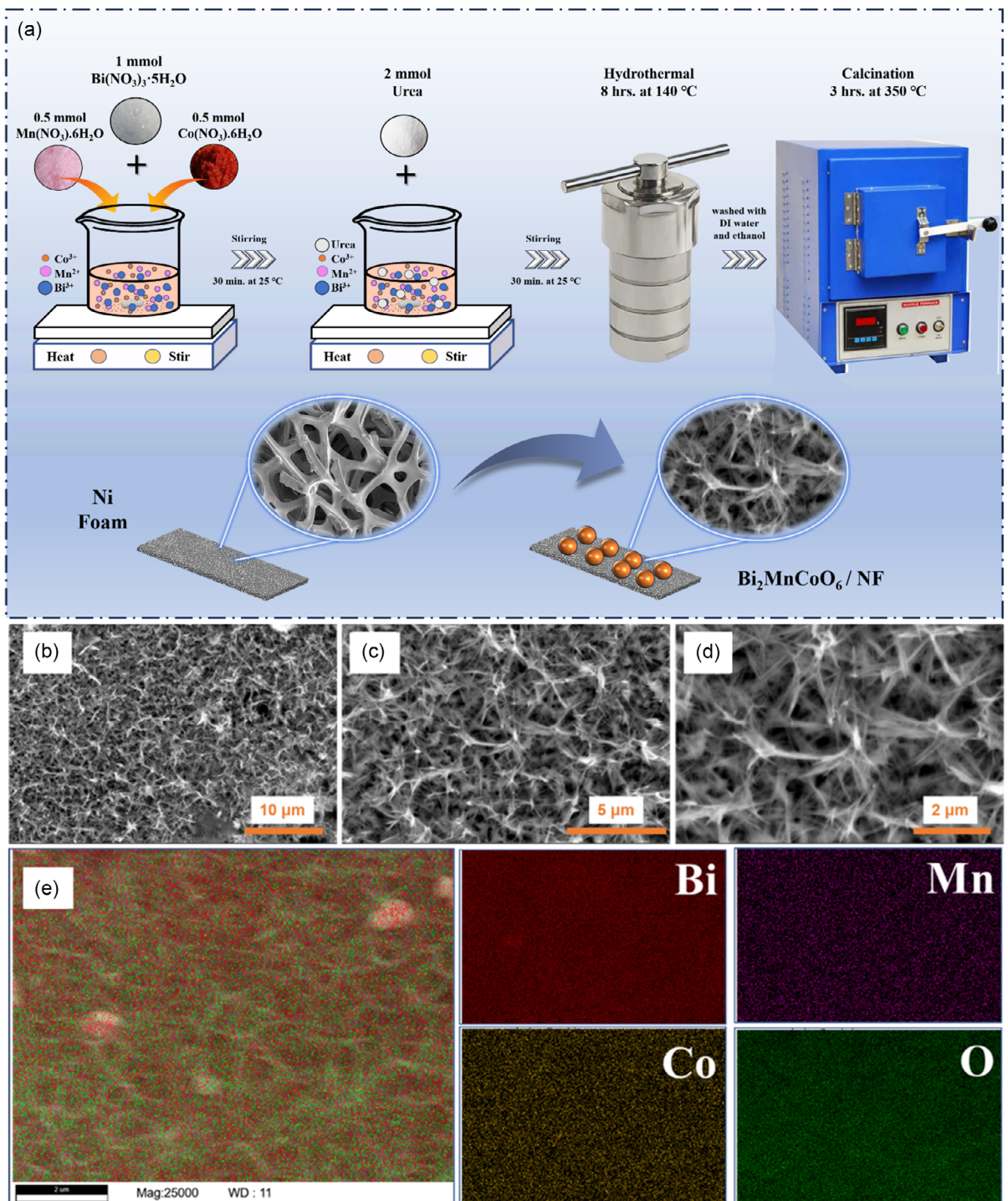


Figure 1. a) Schematic of the hydrothermal route used to synthesize the BMCO sample. b-d) FE-SEM micrographs of BMCO. e) EDS elemental maps for BMCO overlayed (left) and individual distributions of Bi, Mn, Co, and O, demonstrating homogeneous distribution.

electrochemical energy storage applications due to their high surface area and accessible porous structure. These open and interlinked channels can facilitate faster ion diffusion and improve electrolyte penetration during charge/discharge cycles. Figure 1e displays the energy-dispersive X-ray spectroscopy (EDS) elemental mapping images corresponding to the FE-SEM scan,

which confirm the homogeneous distribution of the constituent elements—Bi (red), Mn (purple), Co (yellow), and O (green)—throughout the electrode surface. The even distribution of these elements further verifies the successful synthesis of the BMCO phase and uniform deposition of the active material on the substrate. This uniformity is critical for achieving consistent

electrochemical performance and efficient utilization of the electrode material. Overall, the FE-SEM and EDS mapping results affirm the formation of a highly porous and well-integrated nanostructured BMCO layer, which is expected to contribute positively to the electrochemical performance by providing numerous active sites and enhancing electrolyte–electrode interaction.

High-resolution TEM was employed to investigate the microstructural features and crystallinity of the BMCO nanostructures. At low magnification (Figure 2a), the sample presents as a loosely interconnected network of ultrathin nanorods, suggesting a high degree of porosity. Increasing the magnification (Figure 2b, c)

reveals that these sheets are not entirely amorphous; rather, they comprise numerous nanocrystalline domains embedded within an otherwise disordered matrix. The presence of both ordered and disordered regions is advantageous for facilitating electrolyte infiltration and rapid ion transport. In the high-resolution images (Figure 2d,e), distinct lattice fringes are clearly resolved. Measurement of these fringes yields interplanar spacings of 0.32, 0.29, and 0.26 nm, which correspond precisely to the (310), (222), and (321) planes of the $\text{Bi}_2\text{MnCoO}_6$ double perovskite structure. The ability to observe multiple fringe orientations within single nanorods indicates a polycrystalline nature with a

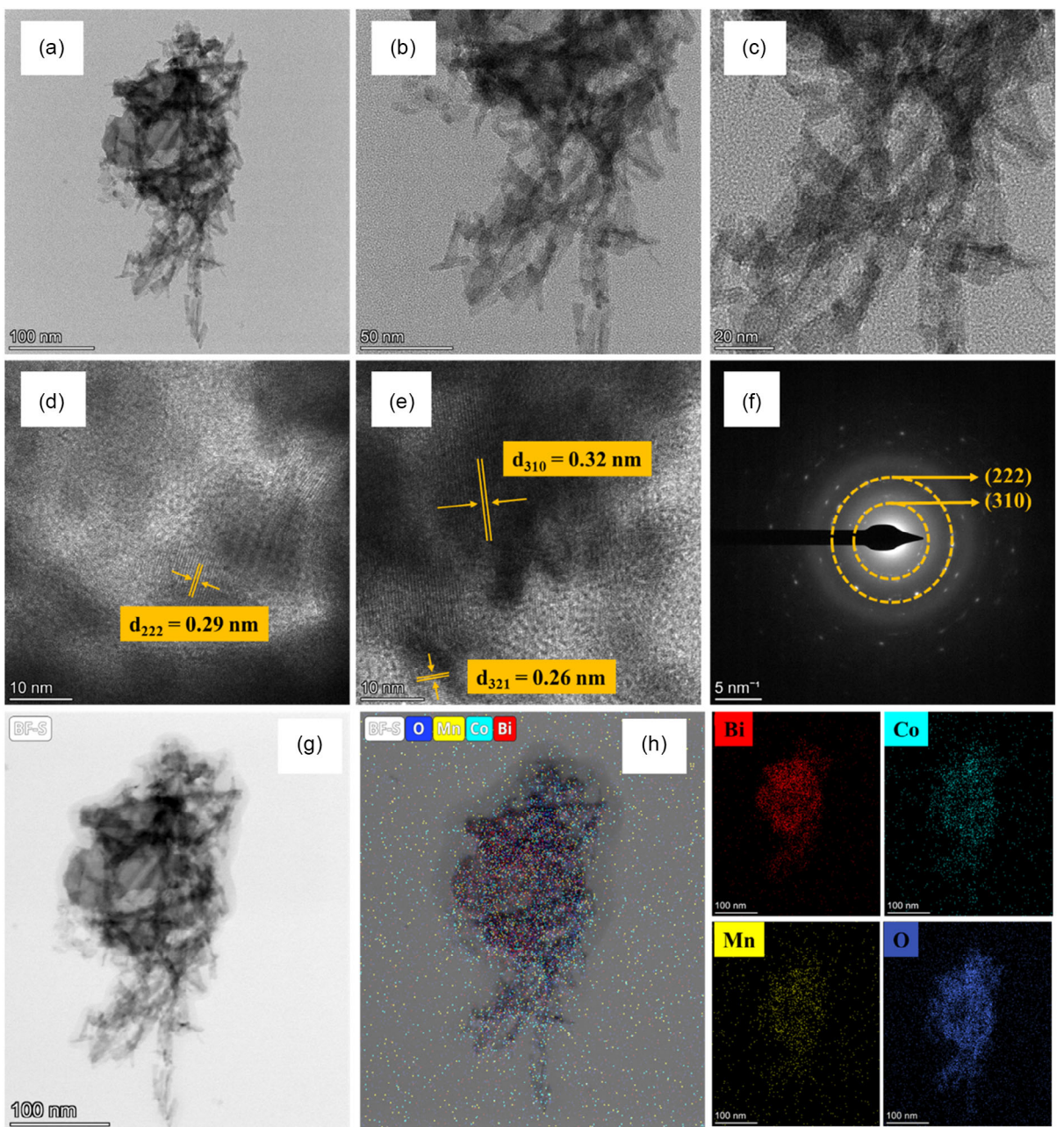


Figure 2. TEM analysis BMCO sample: a–c) low- and high-magnification images d,e) HRTEM micrographs f) SAED pattern g) STEM bright-field image and h) EDS elemental maps for Bi, Mn, Co, and O, demonstrating uniform distribution within the sample.

variety of exposed crystal facets, each providing additional redox-active sites. Selected-area electron diffraction (SAED) patterns (Figure 2f) show sharp, concentric rings indexed to the same (310) and (222) planes, confirming the phase purity and nanocrystalline character of the BMCO. The finite widths of these diffraction rings imply crystallite sizes on the order of 5–10 nm, in excellent agreement with the domain sizes observed in HRTEM images. To verify elemental distribution, bright-field STEM coupled with EDS mapping was performed (Figure 2g, h). The resulting maps demonstrate that Bi, Mn, Co, and O are homogeneously dispersed throughout the nanorods, with no evidence of elemental segregation or secondary-phase formation. Such uniform cation incorporation into the perovskite lattice ensures that all potential redox centers are electrochemically accessible. This uniformity is critical for consistent electrochemical behavior and underscores the effectiveness of the hydrothermal synthesis approach.

3.2. Structural Analysis

The crystalline structure of the synthesized $\text{Bi}_2\text{MnCoO}_6$ (BMCO) was examined using X-ray diffraction (XRD), as shown in Figure 3a. The primary diffraction peaks are well matched with the cubic perovskite phase of BiCoO_3 , in agreement with the standard JCPDS card no. 00-039-1010, confirming the successful formation of the desired cubic phase. Two additional peaks marked with asterisks (#) originate from the underlying Ni foam substrate. The elemental composition of BMCO was further verified by X-ray

photoelectron spectroscopy (XPS), as illustrated in Figure 3b, confirming the presence of Bi, Mn, Co, and O. In the high-resolution Bi 4f spectrum (Figure 3c), the Bi 4f_{7/2} and 4f_{5/2} peaks appear at binding energies of \approx 159.2 and 164.5 eV, respectively.^[41–43] Figure 3d displays the Mn 2p spectrum, with well-defined Mn 2p_{3/2} and Mn 2p_{1/2} peaks at 641.9 and 653.5 eV, respectively. Deconvolution reveals subpeaks corresponding to Mn²⁺ at 641.8 and 653.3 eV, and Mn³⁺ at 644.3 and 654.8 eV, with a spin-orbit splitting of 11.5 eV.^[41,44] The intensity distribution indicates a mixed-valence state dominated by Mn²⁺, which is beneficial for enhancing redox activity. The Co 2p spectrum (Figure 3e) shows two main spin-orbit doublets with a separation of 15.5 eV between Co 2p_{3/2} and Co 2p_{1/2} at 780.2 and 795.0 eV, respectively, with characteristic satellite features confirming the coexistence of Co²⁺ and Co³⁺ oxidation states. Fitting analysis identifies Co²⁺ peaks at 780.1 and 795.30 eV, and Co³⁺ peaks at 781.3 and 796.8 eV.^[41,42,45] Finally, the O 1s spectrum in Figure 3f reveals three distinct peaks: 529.9 eV (lattice oxygen, O_L), 531.2 eV (oxygen vacancies, O_V), and 532.8 eV (surface-adsorbed water, O_C), indicating the complex oxygen environment within the BMCO perovskite structure.^[46,47] The Brunauer–Emmett–Teller surface area analysis, along with pore-size distribution data, is shown in Figure S1, Supporting Information. The sample exhibits a specific surface area of $17.3 \text{ m}^2 \text{ g}^{-1}$, an average pore diameter of 18.9 nm, and a total pore volume of $0.074 \text{ cm}^3 \text{ g}^{-1}$. These results confirm the presence of mesopores that facilitate electrolyte penetration and support the observed enhancement in electrochemical performance.

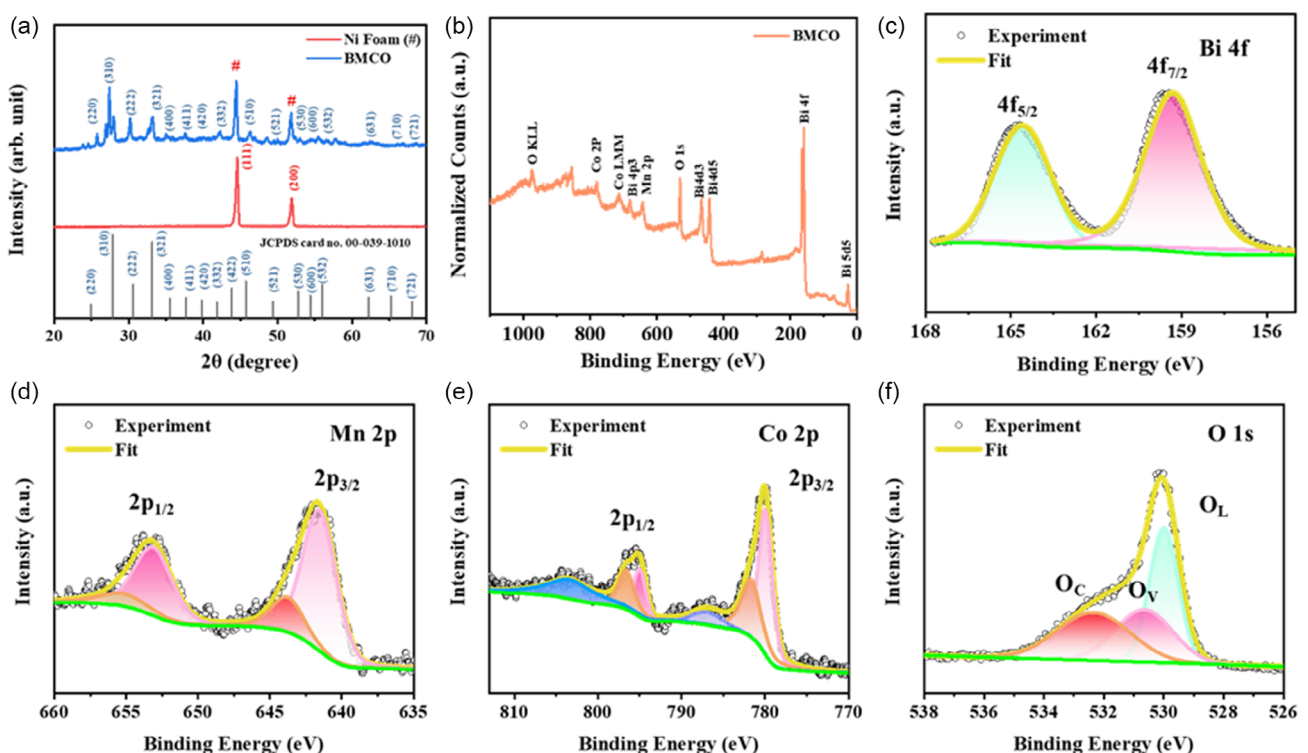


Figure 3. a) XRD of the BMCO sample. b) XPS survey spectrum of BMCO. c–f) deconvoluted high-resolution spectra of Bi 4f, Mn 2p, Co 2p and O 1s.

3.3. Electrochemical Performance Evaluation

The electrochemical behavior of the hydrothermally synthesized BMCO electrode was examined using galvanostatic charge-discharge (GCD), cyclic voltammetry (CV), and electrochemical

impedance spectroscopy (EIS) in a three-electrode setup with 6 M KOH electrolyte. Figure 4a shows CV profiles recorded at various scan rates from 5 to 120 mV s⁻¹. The curves exhibit quasirectangular shapes with weak redox humps, suggesting a combination of EDLC and pseudocapacitance derived from

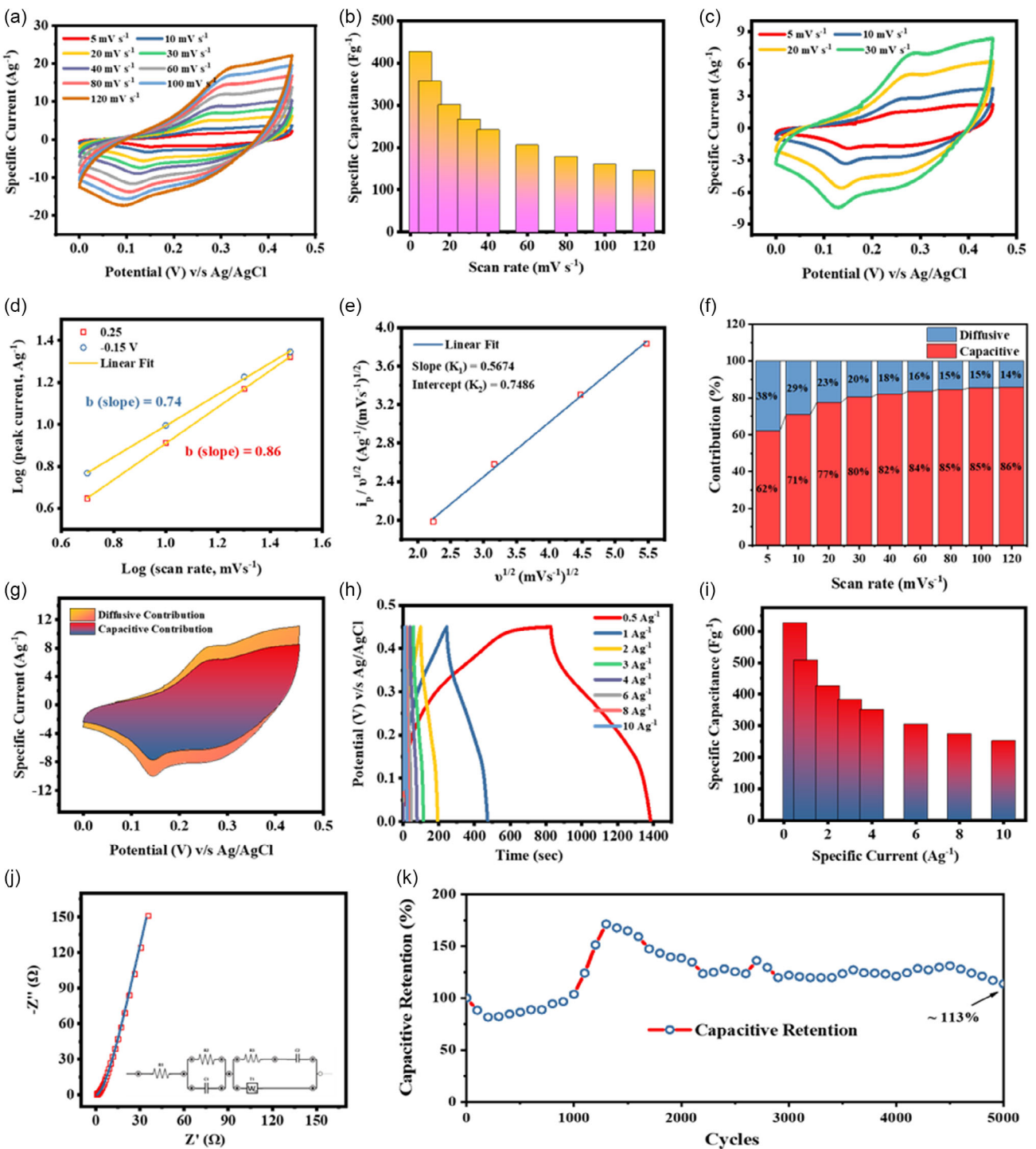
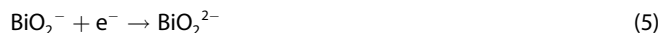


Figure 4. Electrochemical performance of BMCO electrodes tested in a three-electrode setup with 6 M KOH; a) CV curves of the electrode material recorded at various scan rates (5–120 mV s^{-1}); b) specific capacitance vs. scan rate; c) CV profiles recorded at low scan rates (5–30 mV s^{-1}); d) Logarithmic plot of i_p versus $\log v$; e) Plot of $i_p/v^{1/2}$ against $v^{1/2}$; f) Bar graph depicting the relative contributions of diffusive and capacitive mechanisms; g) CV curve at 20 mV s^{-1} illustrating the diffusion-controlled (yellow) and capacitive-controlled (red) contributions; h) GCD profiles at various current densities; i) Specific capacitance vs. current density; j) Nyquist plot with fitted equivalent circuit (inset); and k) Cycling performance over 5000 charge–discharge cycles at 10 A g^{-1} .

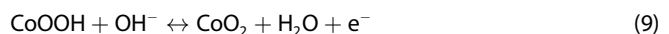
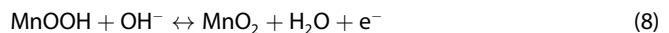
reversible faradaic redox reactions. The increase in current response with increasing scan rate indicates the electrode's ability to deliver high power. However, the distortion in shape at higher scan rates is attributed to insufficient ion diffusion time, especially into the inner pores of the electrode.^[48] The corresponding variation in specific capacitance as a function of scan rate is plotted in Figure 4b. A clear decreasing trend is observed as the scan rate increases, which is a well-known phenomenon in supercapacitors. At lower scan rates, electrolyte ions have ample time to penetrate deeper into the porous structure of the electrode, allowing more active sites to participate in the charge storage process. In contrast, at higher scan rates, the ions are restricted to surface or near-surface regions, resulting in lower accessible surface area and thus reduced specific capacitance. The surface charges on the electrode arise from electrostatic interactions between charged species during the charge-discharge cycles. The distinct redox peaks observed in the CV curves are attributed to reversible Faradaic processes involving redox transitions such as Bi_{metal}/Bi³⁺, Mn²⁺/Mn³⁺, and Co²⁺/Co³⁺ in the presence of KOH electrolyte. These redox reactions are characteristic of the BMCO sample electrodes, and the corresponding anodic peaks are associated with the oxidation of these bimetallic species in the alkaline medium.^[49,50]



The cathodic peaks correspond to the reduction of Bi³⁺ to its lower oxidation state (Bi⁰ or bimetallic form) in the alkaline KOH medium. The likely reduction mechanism can be described by the following reaction



The redox processes involving Mn³⁺/Mn²⁺ and Co³⁺/Co²⁺ in the presence of OH⁻ ions from the KOH electrolyte can be described by the following electrochemical reactions^[51]



The synergistic enhancement of charge storage in BMCO electrodes arises from the coexistence of multiple oxidation states of Bi, Mn, and Co, which results in intersecting and complementary redox reactions across a broader electrochemical potential window. The reversible transformation between various valence states—such as Bi⁰/Bi³⁺, Mn²⁺/Mn³⁺/Mn⁴⁺, and

Co²⁺/Co³⁺/Co⁴⁺—enables several concurrent faradaic processes, thereby increasing the number of active sites available for charge storage and electron transfer. This multivalent redox chemistry not only expands the capacitive response of the electrode but also improves reaction kinetics and charge accumulation capacity, as the simultaneous presence of distinct metal ions facilitates rapid and reversible electron exchange with the electrolyte.^[52] Collectively, these effects account for the observed superior electrochemical performance of BMCO electrodes, providing robust and high-rate charge storage behavior that surpasses systems with a single redox-active component.

To gain a deeper understanding of the charge storage mechanism, Figure 4c shows CV curves at intermediate scan rates (5–30 mV s⁻¹), and the peak current (i_p) values were analyzed against scan rate (v) using the power law relationship,^[53]

$$i_p = av^b \quad (10)$$

$$\log i_p = b \log v + \log a \quad (11)$$

The values of a and b are obtained through linear fitting of the logarithmic plot of peak current (i_p) versus log(scan rate), where the slope gives b and the intercept provides a . As illustrated in Figure 4d, the log-log plots of i_p versus scan rate show distinct anodic and cathodic peaks around 0.25 and -0.15 V, respectively. The calculated b -values from the slopes of these plots are 0.74 and 0.86, suggesting that both diffusion-controlled and capacitive processes contribute to the overall charge storage behavior. A b -value of 0.5 corresponds to a purely diffusion-limited faradaic process, while a value of 1.0 implies a purely capacitive response.^[54,55] These values, which exceed 0.5, highlight the dominance of capacitive processes, reflecting the system's stability. To quantitatively distinguish these contributions, the Dunn model (Equation (12)) was applied, which separates the total current (i_p) into capacitive (k_1v) and diffusion-controlled ($k_2v^{1/2}$) components^[56,57]

$$i_p = k_1v + k_2v^{1/2} \quad (12)$$

Rearranging gives:

$$i_p/v^{1/2} = k_1v^{1/2} + k_2 \quad (13)$$

Figure 4e presents the plot of $v^{1/2}$ and $i_p/v^{1/2}$ for the peak current at 0.25 V. From the linear fit, the slope and intercept yield the values of k_1 and k_2 , representing the capacitive and diffusion-controlled contributions, respectively.

Figure 4f outlines the proportional contributions of capacitance and diffusion computed across various scan rates (ranging from 5 to 120 mV s⁻¹). The capacitive contribution steadily rises from 62% to 86% as the scan rate escalates, signifying a predominantly capacitive charge storage process at higher scan rates. At lower scan rates, ions luxuriate in longer intervals for redox reactions within the material, highlighting an increased diffusive contribution. At higher scan rates, charges gain a competitive edge over ions, finding more chances to adhere to the electrode/electrolyte interface through physical adsorption. This intensifies

the capacitive influence, making a substantial impact on the overall performance spectrum.^[58] The deconvoluted capacitive and diffusive contribution at 10 mV s^{-1} is visually presented in Figure 4g, confirming the mixed charge storage behavior of BMCO. The prevailing capacitive nature within the BMCO sample not only prolongs its cycling durability but also fortifies its adaptability to different charging rates. Its rapid kinetics position it as an ideal candidate for pseudocapacitive electrodes, guaranteeing swift energy exchange—ideal for applications requiring high power output.

Figure 4h presents GCD profiles measured at current densities varying from 0.5 to 10 A g^{-1} . The near-linear and symmetric charge–discharge profiles with negligible voltage drop demonstrate good capacitive behavior and high reversibility of the redox reactions. The derived specific capacitance values from these GCD curves are plotted in Figure 4i, showing a similar decreasing trend with increasing current density. This is because of the following reasons may be involved: 1) At higher current densities, ion diffusion within the electrode pores may not match the rapid charge–discharge rate, resulting in concentration polarization. 2) A high volume of micropores can create extended ion transport paths, making it difficult for electrolyte ions to access these pores efficiently at fast scan rates. 3) The pseudocapacitive nature of BMCO requires sufficient time for redox reactions, which may be incomplete at high current densities, leading to a partial loss in capacitance. 4) As the current increases, the relative contribution of pseudocapacitance diminishes while electric double-layer capacitance becomes dominant, reducing the total capacitance and altering the discharge profile.

EIS analysis is shown in Figure 4j. The Nyquist plot reveals a small semicircle in the high-frequency region and a near-vertical line in the low-frequency region, suggesting low equivalent series resistance ($R_s = 0.57 \Omega$) and charge transfer resistance ($R_{ct} = 1.80 \Omega$) and ideal capacitive behavior. The equivalent circuit model inset confirms the presence of low internal resistance and favorable ion transport dynamics, which are crucial for high-performance supercapacitor electrodes.

The long-term cycling stability of the BMCO electrode was evaluated by repeated galvanostatic charge–discharge at 10 A g^{-1} over 5,000 cycles (Figure 4k). An initial slight drop in specific capacitance to $\approx 85\%$ of the starting value is observed within the first few hundred cycles, likely due to electrode/electrolyte equilibration. Remarkably, this is followed by a pronounced “self-activation” phase: the capacitance climbs to a maximum of $\approx 165\%$ by $\approx 1,200$ cycles, indicating progressive penetration of previously inaccessible pores and the gradual activation of additional redox-active sites. Beyond this peak, the capacitance gently declines and stabilizes around $\approx 120\text{--}130\%$ for the next 2,000 cycles, demonstrating the material’s robustness. From $\approx 3,000$ to 5,000 cycles, the ASC maintains $\approx 113\%$ of its initial capacitance, highlighting exceptional long-term durability. Overall, the electrode has outstanding stability, with $>110\%$ capacitance retention after 5,000 cycles and no sign of accelerated degradation. The selection of a charge–discharge current density of 10 A g^{-1} for the cycling stability test of the BMCO electrode was based on both scientific and practical considerations.

First, cycling at a high current density provides a stringent condition that accelerates electrode degradation, thereby serving as a robust means to assess long-term durability under demanding operational regimes. This approach offers a realistic indication of the electrode’s endurance in high-power applications requiring rapid charge–discharge performance. Second, practical time constraints played a significant role. The BMCO electrode, owing to its high capacitance, would require ≈ 695 h to complete 5,000 cycles at a lower current density of 1 A g^{-1} . By conducting the long-term stability test at 10 A g^{-1} , the total cycling time is significantly reduced to about 40 h, which enables efficient yet rigorous evaluation and ensures the feasibility of comprehensive stability testing within available laboratory resources. Additionally, repeat stability tests were also performed at an even higher current density of 15 A g^{-1} , as shown in Figure S2, Supporting Information. This comparative testing further strengthens the analysis by demonstrating cycling performance and confirming the robustness of the BMCO electrode under increasingly demanding conditions. The combined testing at different current densities provides a more complete evaluation of the electrode’s cycling stability under a range of practical use cases.

The self-activation phenomenon observed in our BMCO//AC ASC device is further supported by FESEM imaging conducted before and after extensive cycling, as shown in Figure S3, Supporting Information. Initial micrographs show a highly porous, interconnected nanofibrous network that facilitates electrolyte penetration and hosts “hidden” redox sites. After cycling, a pronounced structural evolution to a denser, blade- or nanorod-like morphology is evident, indicating surface reconstruction that exposes additional active redox sites and enhances specific surface area. This morphological transformation directly corroborates the electrolyte-driven activation process and rationalizes the $>150\%$ capacitance retention observed in the early cycles. Analogous phenomena have been noted in other systems where structural evolution (e.g., petal-like, flower-like, or blade-like morphologies) after cycling results in enhanced capacitance due to increased specific surface area and improved ion transport pathways.^[59] Table S1, Supporting Information summarizes related literature reports, demonstrating that such self-activation is a common and intrinsic characteristic among advanced electrode architectures. These morphological and electrochemical observations together provide clear evidence for the self-activation mechanism in BMCO-based ASC devices.

Such behavior—combining initial activation and sustained retention—is highly desirable for practical supercapacitor applications, ensuring reliable performance over prolonged use. This superior performance can be attributed to the robust double perovskite structure, uniform elemental distribution, and interconnected porous morphology, which together enable rapid ion/electron transport and effective stress accommodation during prolonged cycling. In summary, the electrochemical measurements confirm that the BMCO electrode exhibits a synergistic combination of high specific capacitance, excellent rate capability, low resistance, and outstanding cycling performance, making it a promising candidate for high-performance supercapacitor applications.

An ASC device was assembled using $\text{Bi}_2\text{MnCoO}_6$ (BMCO) as the positive electrode and AC as the negative electrode on nickel-foam current collectors in 6 M KOH (Figure 5a).

Designing an efficient ASC requires careful consideration of the charge balance between the cathode and anode to ensure optimal electrochemical performance. This involves matching

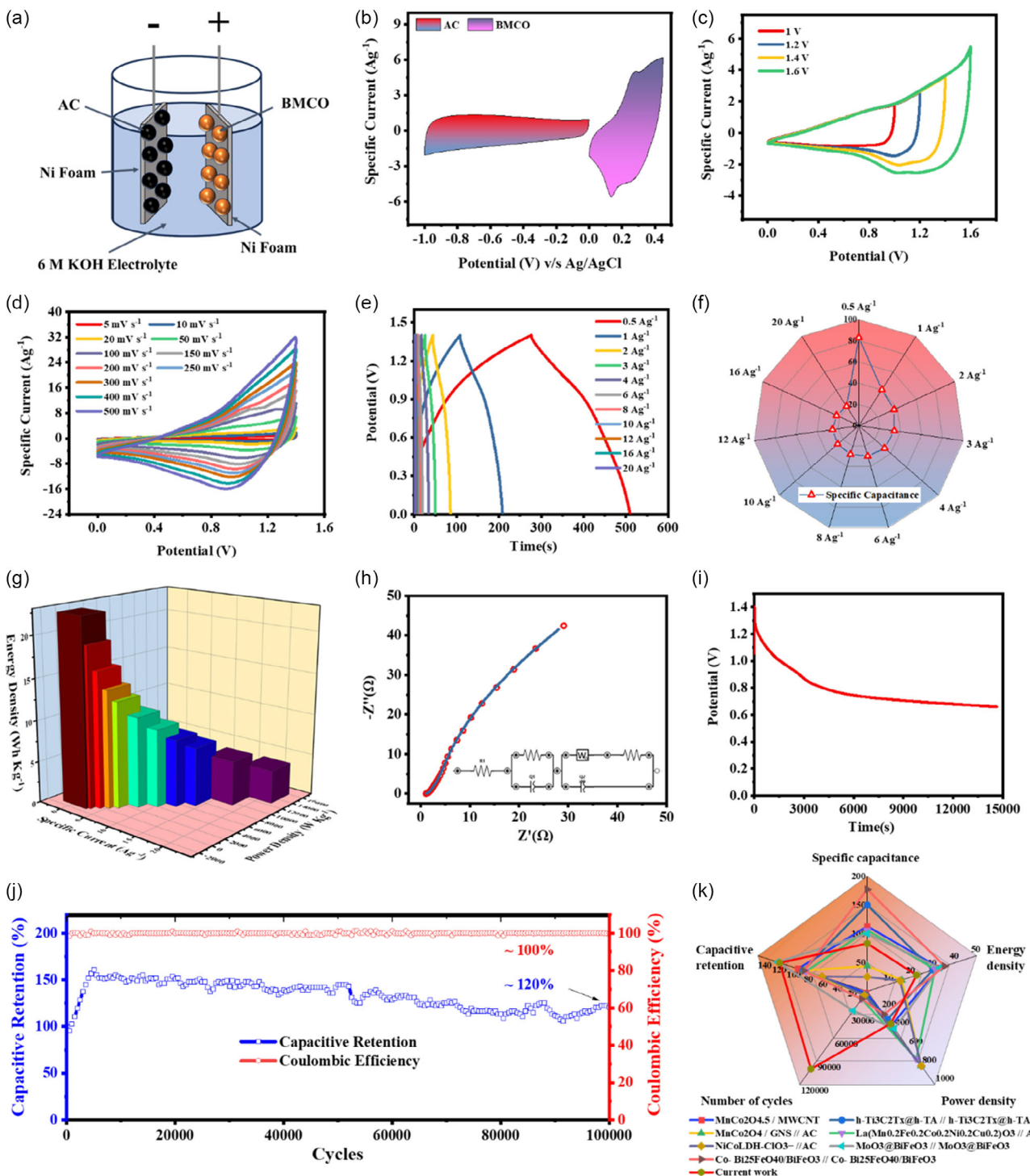


Figure 5. Electrochemical characterization of the ASC with BMCO as the cathode, AC as the anode, and 6 M KOH; a) schematic of the ASC configuration; b) CV curves of BMCO and AC electrodes recorded in a three-electrode setup at a scan rate of 5 mV s^{-1} ; c) CV profiles at various voltage windows; d) CV profiles at various scan rates; e) GCD curves recorded at multiple current densities; f) specific capacitance values at various current densities; g) bar graph illustrating the relationship between energy density and power density at different current densities; h) nyquist plots showing impedance characteristics, with experimental and fitted data, and the corresponding equivalent circuit diagram; i) long-term floating test; j) cycling performance over 100,000 cycles at 10 A g^{-1} ; and k) performance comparison of the BMCO-based ASC.

the charges stored in both electrodes, which can be achieved by adjusting the mass ratio of the active materials. The charge stored (Q) in an electrode is determined by the equation:

The calculation involved determining the stored charge (Q) at each electrode.

$$Q = C \times \Delta V \times m \quad (14)$$

The active mass, specific capacitance, and potential window are denoted by m , C , and ΔV , respectively.

The charge balance equation provided by the following equation enabled the attainment of the mass balance $Q_+ = Q_-$.

$$\frac{m_+}{m_-} = \frac{C_- \times \Delta V_-}{C_+ \times \Delta V_+} \quad (15)$$

For the positive and negative electrode, the numerical values are ($C_+ = 500 \text{ F g}^{-1}$ at 1 A g^{-1} , $V_+ = 0.45 \text{ V}$) and ($C_- = 221 \text{ F g}^{-1}$ at 1 A g^{-1} , $V_- = 1.0 \text{ V}$). By inputting these values into (Equation 16), the calculated mass ratio (m_+/m_-) for the ASC is found to be 0.88.

The individual CV responses of BMCO and AC (Figure 5b) confirm complementary potential windows: BMCO exhibits redox peaks between 0 and 0.45 V, while AC displays an almost rectangular double-layer profile from -1.0 to 0 V. When combined, the ASC safely operates up to 1.4 V (Figure 5c), with quasirectangular CV curves and well-defined redox signatures at scan rates up to 500 mV s^{-1} (Figure 5d), indicating excellent rate capability and minimal polarization.

GCD measurements (Figure 5e) show nearly symmetric triangular profiles with small IR drops at current densities from 0.5 to 20 A g^{-1} . The C_s calculated from these GCD curves decreases from $\approx 83 \text{ F g}^{-1}$ at 0.5 A g^{-1} to $\approx 15 \text{ F g}^{-1}$ at 20 A g^{-1} (radar plot, Figure 5f), retaining $\approx 18\%$ of the low-rate capacitance at the highest current. The Ragone-type 3D bar chart (Figure 5g) reveals a maximum energy density of $\approx 23 \text{ Wh kg}^{-1}$ at a power density of $\approx 347 \text{ W kg}^{-1}$, decreasing to $\approx 4 \text{ Wh kg}^{-1}$ at 14 kW kg^{-1} , demonstrating a favorable trade-off for practical applications. EIS (Figure 5h) yields a small solution resistance ($\approx 1.06 \Omega$) and a low charge-transfer resistance ($\approx 0.62 \Omega$), evidencing fast ion transport and efficient interfacial kinetics. A long-term floating test at 1.5 V (Figure 5i) shows negligible voltage decay over 15,000 s, further confirming stability under bias.

To assess the durability of the BMCO//AC ASC device under extreme cycling demands, galvanostatic charge-discharge tests were carried out at 10 A g^{-1} for 100,000 cycles (Figure 5j). The Coulombic efficiency (red circles) remains nearly 100% throughout, indicating highly reversible charge-discharge processes with negligible parasitic reactions. The capacitive retention (blue squares) exhibits an initial activation phase: within the first $\approx 10,000$ cycles, the capacitance rises rapidly to $\approx 150\%$ of its original value, reflecting progressive infiltration of electrolyte into previously inaccessible pores and the activation of additional redox-active sites. Following this peak, the retention undergoes a gradual decrease, stabilizing around 120% by the 1,00,000th cycle. Remarkably, even after 100 k cycles, the device retains well

over 100% of its initial capacitance. This exceptional stability can be attributed to several factors: 1) The hierarchical porosity and strong adhesion of BMCO on nickel foam resist mechanical degradation. 2) Progressive infiltration of electrolyte into previously inaccessible pores and the activation of additional redox-active sites over extended cycling. 3) The PVA-KOH gel electrolyte maintains ionic conductivity without causing electrode dissolution or passivation.

Overall, the ASC device demonstrates outstanding long-term reliability, combining high Coulombic efficiency with increasing and then sustained capacitive retention. Such performance is highly desirable for practical supercapacitor applications, ensuring both longevity and stable high-power delivery. As depicted in the comparative radar chart (Figure 5k), the BMCO//AC device stands out in terms of cycling stability and capacitance retention, outperforming many reported systems.^[38,46,60–63] While the energy and power densities are moderate relative to some literature examples, the overall balance of performance highlights the strong potential of the BMCO//AC configuration for reliable, high-cycle-life supercapacitor applications.

4. Conclusion

In summary, we have successfully synthesized a bismuth-based double perovskite, $\text{Bi}_2\text{MnCoO}_6$ (BMCO), via a cost-effective and environmentally friendly hydrothermal route, and demonstrated its potential as a high-performance supercapacitor electrode. The strategic incorporation of Bi^{3+} at the A-site and the synergistic redox activity of Mn and Co at the B-site enable enhanced electronic conductivity and rich pseudocapacitive behavior. BMCO exhibits a remarkable specific capacitance of 627 F g^{-1} in a three-electrode setup, along with excellent rate capability and reversibility. When integrated into an ASC (BMCO//AC) with AC as the anode and 6 M KOH as the electrolyte, the device delivers a high energy density of 23 Wh kg^{-1} and a power density of 14 kW kg^{-1} . Notably, the ASC device demonstrates outstanding long-term cycling stability, retaining $\approx 120\%$ of its initial capacitance even after 100,000 charge-discharge cycles, with $\approx 100\%$ Coulombic efficiency. The initial "self-activation" phenomenon—wherein the capacitance surges to 150% in the early 10,000 cycles—is attributed to progressive electrolyte infiltration and activation of deep redox-active sites. Superior cycling stability, confirmed via the radar chart, places BMCO//AC among the most robust systems reported, particularly in terms of longevity, while maintaining moderate energy and power performance. Overall, this work sets a new benchmark for perovskite-based energy storage systems and underscores the potential of cation-engineered double perovskites, like BMCO, in delivering highly stable and efficient supercapacitor devices. The combination of simple synthesis, structural versatility, and exceptional electrochemical durability makes BMCO a promising candidate for next-generation energy storage applications.

Acknowledgements

S.K.M. and D.K. gratefully acknowledge the Council of Scientific and Industrial Research (CSIR), India, for providing research funding. A.M. acknowledges the Ministry of Education (MoE), Government of India, for supporting his research through the Prime Minister's Research Fellowship (PMRF).

Conflict of Interest

The authors declare no conflict of interest.

Author Contributions

Shivam Kumar Mittal: conceptualization, methodology, formal analysis, electrode fabrication, device fabrication, investigation, writing—original draft. **Amiya Mandal:** conceptualization, writing—review & editing. **Deepanshu Kaneria:** conceptualization, writing—review & editing. **Udeshwari Jamwal:** formal analysis, writing—review & editing. **Kanhaiya Lal Yadav:** supervision, writing—review & editing, resources.

Data Availability Statement

The data that support the findings of this study are available from the corresponding author upon reasonable request.

Keywords: asymmetric supercapacitor • $\text{Bi}_2\text{MnCoO}_6$ • double perovskite • hydrothermal method • stability

- [1] A. S. Raja, R. Sasikumar, S. Chen, B. Kim, *Small* **2025**, *21*, e2411728.
- [2] T. Ahmad, D. Zhang, *Energy Rep.* **2020**, *6*, 1973.
- [3] Z. Ji, G. Tang, J. Zhang, X. Chuan, J. Zhong, Z. Lin, P. Song, K. Xu, X. Shen, *Chem. Eng. J.* **2024**, *501*, 157619.
- [4] X. Tian, Q. Wang, J. Yang, R. Luo, X. Zhang, S. Xue, Y. Shi, W. Hu, Z. Liu, *J. Power Sources* **2025**, *632*, 236377.
- [5] J. Xiong, L. Lou, X. Yan, R. Xie, Z. Wang, X. Liu, P. Zhou, Q. Guo, H. Shi, X. Ge, *J. Power Sources* **2025**, *640*, 236758.
- [6] Y. Yang, B. Chen, Y. Zhang, H. Peng, J. Chen, S. Chen, *ACS Appl. Mater. Interfaces* **2024**, *16*, 42502.
- [7] H. Xu, H. Dong, X. Liu, H. Qiao, G. Chen, F. Du, Y. Dall'Agnese, Y. Gao, *ACS Appl. Mater. Interfaces* **2023**, *15*, 53549.
- [8] W. Bi, J. Wang, E. P. Jahrman, G. T. Seidler, G. Gao, G. Wu, G. Cao, *Small* **2019**, *15*, 1901747.
- [9] X. Qiu, N. Wang, Z. Wang, F. Wang, Y. Wang, *Angew. Chem.—Int. Ed.* **2021**, *60*, 9610.
- [10] T. Lv, Y. Yao, N. Li, T. Chen, *Angew. Chem. Int. Ed.* **2016**, *55*, 9191.
- [11] D. M. Saju, R. Sapna, U. Deka, K. Hareesh, *J. Power Sources* **2025**, *647*, 237302.
- [12] M. A. Irham, R. D. Septianto, R. D. Wulandari, Y. Majima, F. Iskandar, Y. Iwasawa, S. Z. Bisri, *ACS Appl. Mater. Interfaces* **2024**, *16*, 24889.
- [13] P. Zhang, M. Wang, Y. Liu, Y. Fu, M. Gao, G. Wang, F. Wang, Z. Wang, G. Chen, S. Yang, Y. Liu, R. Dong, M. Yu, X. Lu, X. Feng, *J. Am. Chem. Soc.* **2023**, *145*, 6247.
- [14] K. Wang, H. Wu, Y. Meng, Z. Wei, *Small* **2014**, *10*, 14.
- [15] R. Mohanty, A. Nashim, K. Parida, *Small* **2025**, *21*, 2506223.
- [16] M. Guo, J. Balamurugan, X. Li, N. H. Kim, J. H. Lee, *Small* **2017**, *13*, 1701275.
- [17] M. Ö. A. Çolak, A. L. Passos, A. Güngör, E. Erdem, R. Genç, *J. Power Sources* **2025**, *645*, 237230.
- [18] L. Liu, S. Zuo, S. Wang, *Chem. Eng. J.* **2024**, *502*, 158052.
- [19] M. Harilal, S. G. Krishnan, A. Yar, I. I. Misnon, M. V. Reddy, M. M. Yusoff, J. O. Dennis, R. Jose, *J. Phys. Chem. C* **2017**, *121*, 21171.
- [20] Z. Fahimi, O. Moradlou, A. Sabbah, K. H. Chen, L. C. Chen, M. Qorbani, *Chem. Eng. J.* **2022**, *436*, 135225.
- [21] M. Mushtaq, Z. Zhu, H. Yang, Z. Khanam, Y. wen Hu, S. Mathi, Z. Wang, M. S. Balogun, Y. Huang, *Small* **2025**, *21*, 2409418.
- [22] L. Zhu, Y. Liu, C. Su, W. Zhou, M. Liu, Z. Shao, *Angew. Chemie—Int. Ed.* **2016**, *55*, 9576.
- [23] J. T. Mefford, W. G. Hardin, S. Dai, K. P. Johnston, K. J. Stevenson, *Nat. Mater.* **2014**, *13*, 726.
- [24] K. Moorthi, B. Sivakumar, B. Chokkiah, H. Valdes, S. Mohan, *ACS Appl. Nano Mater.* **2023**, *7*, 18511.
- [25] Z. Meng, J. Xu, P. Yu, X. Hu, Y. Wu, Q. Zhang, Y. Li, L. Qiao, Y. Zeng, H. Tian, *Chem. Eng. J.* **2020**, *400*, 125966.
- [26] M. Alam, K. Karmakar, M. Pal, K. Mandal, *RSC Adv.* **2016**, *6*, 114722.
- [27] L. Shen, L. Yu, X. Y. Yu, X. Zhang, X. W. D. Lou, *Angew. Chemie Int. Ed.* **2015**, *54*, 1868.
- [28] S. Y. Khan, T. Noor, N. Iqbal, Z. Ali, *Mater. Res. Bull.* **2025**, *183*, 113189.
- [29] J. Lee, Y. Shin, T. Kim, W. Choi, M. H. Jung, Y. M. Kim, K. J. Yoon, H. Y. Jeong, D. Lee, J. H. Joo, *Chem. Mater.* **2024**, *36*, 2933.
- [30] V. V. Deshmukh, H. V. Harini, H. P. Nagaswarupa, R. Naik, C. R. Ravikumar, *J. Energy Storage* **2023**, *68*, 107805.
- [31] A. Arya, S. Tanwar, M. Iqbal, A. Sharma, A. L. Sharma, *J. Energy Storage* **2025**, *105*, 114778.
- [32] W. Du, D. Fan, J. Fan, *Ceram. Int.* **2024**, *50*, 10667.
- [33] M. Liu, R. Ding, Y. Li, A. Wang, F. Yang, Y. Zhang, Q. Fang, M. Yan, J. Xie, Z. Chen, Z. Yan, Y. He, J. Guo, X. Sun, E. Liu, *Energy Storage Mater.* **2023**, *63*, 103004.
- [34] Q. Pan, C. Yang, Q. Jia, W. Qi, H. Wei, M. Wang, S. Yang, B. Cao, *Chem. Eng. J.* **2020**, *397*, 125524.
- [35] S. Yin, Y. Wu, J. Chen, Z. Chen, H. Hou, Q. Liu, Y. Wang, W. Zhang, *Funct. Mater. Lett.* **2018**, *11*, 1850013.
- [36] F. Wang, H. Yang, H. Zhang, J. Su, X. Wang, *J. Electron. Mater.* **2017**, *46*, 182.
- [37] N. Matinise, N. Botha, I. G. Madiba, M. Maaza, *MRS Adv.* **2023**, *8*, 703.
- [38] S. K. Rout, P. K. Samal, J. Panigrahy, P. Nanda, S. Praharaj, D. Rout, *J. Alloys Compd.* **2025**, *1020*, 179422.
- [39] Z. Pei, K. Leng, W. Xia, Y. Lu, H. Wu, X. Zhu, *J. Magn. Magn. Mater.* **2020**, *508*, 166891.
- [40] L. Sahoo, S. A. Behera, P. G. R. Achary, S. K. Parida, *Mater. Adv.* **2025**, *6*, 1455.
- [41] S. K. Mittal, U. Jamwal, D. Yadav, D. Kaneria, A. Narwal, K. Kukreti, K. L. Yadav, *IEEE Trans. Dielectr. Electr. Insul.* **2024**, *31*, 1119.
- [42] X. Chen, X. Li, Y. Peng, H. Yang, Y. Tong, M.-S. Balogun, Y. Huang, X. Chen, X. Li, Y. Peng, Y. Huang, H. Yang, M.-S. Balogun, *Adv. Funct. Mater.* **2025**, *35*, 2416091.
- [43] Y. Chen, J. Huang, J. Zhou, X. Li, H. Yang, Y. Huang, *Mater. Today Adv.* **2025**, *25*, 100554.
- [44] S. S. Shalini, Y. P. Fu, A. C. Bose, *Chem. Eng. J.* **2024**, *500*, 156751.
- [45] A. Narwal, S. K. Mittal, K. Kukreti, A. Khokhar, K. L. Yadav, *J. Energy Storage* **2025**, *124*, 116865.
- [46] S. K. Mittal, S. Saini, U. Jamwal, D. Yadav, D. Kaneria, K. L. Yadav, *J. Phys. Chem. C* **2025**, *129*, 61.
- [47] L. Zhu, F. Li, T. Yao, T. Liu, J. Wang, Y. Li, H. Lu, R. Qian, Y. Liu, H. Wang, *Energy Fuels* **2020**, *34*, 11574.
- [48] P. S. Shukla, A. Agrawal, A. Gaur, G. D. Varma, *J. Energy Storage* **2023**, *59*, 106580.
- [49] J. Khajonrit, U. Wongpratit, P. Kidkhunthod, S. Pinitsoontorn, S. Maensiri, *J. Magn. Magn. Mater.* **2018**, *449*, 423.
- [50] J. Cao, J. Li, L. Li, Y. Zhang, D. Cai, D. Chen, W. Han, *ACS Sustain. Chem. Eng.* **2019**, *7*, 10699.
- [51] C. Wang, Y. Liu, Y. Sun, L. Cui, J. Liu, *J. Mater. Chem. A* **2023**, *11*, 7639.
- [52] Z. Li, Y. Niu, X. He, Y. Hu, F. Li, X. Chen, Z. Wang, J. Jiang, C. Wang, *J. Mater.* **2023**, *9*, 62.
- [53] J. Liu, J. Wang, C. Xu, H. Jiang, C. Li, L. Zhang, J. Lin, *Adv. Sci.* **2018**, *5*, 1700322.
- [54] D. D. Farashah, M. Abdollahi, A. M. Zardkhoshouei, S. S. H. Davarani, *Nanoscale* **2024**, *16*, 8650.
- [55] T. Brezesinski, J. Wang, S. H. Tolbert, B. Dunn, *Nat. Mater.* **2010**, *9*, 146.
- [56] J. Wang, J. Polleux, J. Lim, B. Dunn, *J. Phys. Chem. C* **2007**, *2*, 14925.
- [57] W. Peng, K. Chen, S. Li, J. Wang, Z. Su, N. Song, C. Zhang, S. Luo, A. Xie, *Diam. Relat. Mater.* **2022**, *128*, 109266.
- [58] M. Zahid, M. Muhammad, M. Sulman, S. Ramsha, A. Muhammad, M. Arshad, T. Alharbi, *J. Energy Storage* **2020**, *29*, 101324.

- [59] C. Hsiao, C. Lee, N. Tai, *J. Energy Storage* **2022**, *46*, 103805.
- [60] M. Lai, C. Zhao, D. Wang, R. Gao, P. Cai, L. Sun, Q. He, H. Peng, H. Zhang, F. Xu, C. Hu, K. Liang, C. J. Zhang, *ACS Appl. Mater. Interfaces* **2024**, *16*, 55568.
- [61] L. Zhang, J. Zhang, J. Wang, S. Zhang, H. Xie, Z. Gu, *Chem. Eng. J.* **2025**, *511*, 162080.
- [62] Y. Selvaraj, H. Kuzhandaivel, K. S. Nallathambi, V. Elayappan, *Energy Fuels* **2023**, *37*, 8624.
- [63] Y. Wang, J. Liu, H. Cao, J. Ding, N. Wang, C. He, Y. Zhang, *Chem. Eng. J.* **2025**, *509*, 161246.

Manuscript received: September 9, 2025

Revised manuscript received: October 7, 2025

Version of record online:
